Black Hole Shadows

Alejandro José Florido Tomé   María Hernández Fernández

Mauricio Posner   Héctor Sanchis Pérez

Juan Francisco Vallalta Rueda

January 2024

Contents

1 Introduction

In this work, different kind of black holes (BH) will be studied. This astronomical object has a gravitational pull extremely strong that nothing, not even light, can escape it. Its "surface" (event horizon) defines the boundary where the velocity needed to escape exceeds the speed of light. Matter and radiation fall in, but they can't get out. There are two main classes of black holes have been observed:

- Stellar-mass BH: three to dozens of times the Sun's mass. Spreaded throughout our Milky Way galaxy.

- Supermassive BH: weighting 100,000 to billions of solar masses are found in the centers of most big galaxies, ours included.

Along the work, Schwarzschild, Kerr, Charged and mimickers black holes will be simulated to compare the results an experimental supermassive black hole. The conclusion is that the shadow and background is well described by the Kerr BH.

2 Goals

- Study in depth different types of black holes (Schwarzschild, Kerr, charged and mimicker).

- Simulate some scenarios associated with four types of BH. Model the trajectories of photons generated at different points for all the cases using PyHole distribution as well as analyze and compare some parameters.

- Study and analyze the black hole shadow parameters of M87* using the information collected by the Event Horizon Telescope.

3 Schwarzschild Black Holes

3.1 Theoretical background

3.1.1 The metric

With the exception of Minkowski space, the most important such solution is that discovered by Schwarzschild, which describes spherically symmetric vacuum spacetime. It is the unique solution (of this kind) to Einstein's equations in vacuum.

"Spherically symmetric" means "having the same symmetries as a sphere" (S2). Symmetries of the metric are given by the existence of Killing vectors, therefore, a spherically symmetric manifold is one that has three Killing vector fields which are just like those on S2 and the algebra generated by the vectors is the same. The commutation relations are exactly those of SO(3), the group of rotations in three dimensions.

The most important use of a spherically symmetric vacuum solution is to represent the spacetime outside a star or planet or something like that.

Since we are in vacuum, Einstein's equations become $R_{\mu\nu} = 0$, and following some steps we can obtain the Schwarzschild metric:

$$\mathrm{d}s^2 = -\left(1 - \frac{2GM}{r}\right)\mathrm{d}t^2 + \left(1 - \frac{2GM}{r}\right)^{-1}\mathrm{d}r^2 + r^2\mathrm{d}\Omega^2, \qquad (1)$$

This is true for any spherically symmetric vacuum solution to Einstein's equations; M is interpreted as the conventional Newtonian mass that we would measure by studying orbits at large distances from the gravitating source. Note that as $M \to 0$ we recover Minkowski space, which is to be expected. Note also that the metric becomes progressively Minkowskian as we go to $r \to \infty$; this property is known as *asymptotic flatness*.

The fact that the Schwarzschild metric is not just a good solution, but is the unique spherically symmetric vacuum solution, is known as *Birkhoff's theorem*. It is interesting to note that the result is a static metric. The source must be spherically symmetric, like a collapsing star.

From the form of Eq. (1), the metric coefficients become infinite at $r = 0$, and $r = 2GM$ where an apparent sign tell us that something is going wrong. The metric coefficients, of course, are coordinate-dependent quantities, and it is certainly possible to have a "coordinate singularity" which results from a breakdown of a specific coordinate system rather than the underlying manifold. An example occurs at the origin of polar coordinates in the plane, where the metric $ds^2 = dr^2 + r^2 d\theta^2$ becomes degenerate and the component $g^{\theta\theta} = r^{-2}$ of the inverse metric blows up, even though that point of the manifold is no different from any other.

This can be analysed using the Riemann tensor. From the curvature we can construct various scalar quantities meaningful to say that they become infinite. This simplest such scalar is the Ricci scalar $R = g\mu\nu R_{\mu\nu}$. If any of these scalars go to infinity as we approach some point, we will regard that point as a singularity of the curvature.

In the case of the Schwarzschild metric, direct calculation reveals that:

$$R^{\mu\nu\rho\sigma} R_{\mu\nu\rho\sigma} = \frac{12G^2 M^2}{r^6}, \tag{2}$$

At the other trouble spot, $r = 2GM$, it is easy to see that none of the curvature invariants blows up. The surface $r = 2GM$ is very well-behaved (although interesting) in the Schwarzschild metric.

Another important aspect of a Schwarzschild's black hole is the event horizon boundary. For a rotating black hole there are an outer and inner radius, that coincide for the Schwarzschild case. Inside the event horizon's radius, nothing cannot escape (not even light) from the black hole.

The Schwarzschild radius, R_s, is the radius of the event horizon for a non-rotating, uncharged black hole. It is defined as:

$$R_s = \frac{2GM}{c^2}, \tag{3}$$

These black holes also have a photon sphere (a region of space where gravity is so strong that photons are forced to travel in orbits). The radius of the photon sphere, is, for a Schwarzschild black hole:

$$R = \frac{3R_s}{2}, \tag{4}$$

3.1.2 Symmetries and orbits

Killing vectors represent symmetries that are also present in flat spacetime. Invariance under time translations leads to conservation of energy, while invariance under spatial rotations leads to conservation of the three components of angular momentum. We can think of the angular momentum as a three-vector with a magnitude (one component) and direction (two components). Conservation of the direction of angular momentum means that the particle will move in a plane. We can choose this to be the equatorial plane of our coordinate system. Thus, the two Killing vectors which lead to conservation of the direction of angular momentum imply: $\theta = \pi/2$. Together these conserved quantities provide a convenient way to understand the orbits of particles in the Schwarzschild geometry.

Circular orbits will be stable if they correspond to a minimum of the potential, and unstable if they correspond to a maximum. Bound orbits which are not circular will oscillate around the radius of the stable circular orbit. They appear at:

$$r_c = \frac{L^2}{\epsilon GM},$$

(5)

For massless particles $\epsilon = 0$, and there are no circular orbits. Although it is somewhat obscured in this coordinate system, massless particles actually move in a straight line, since the Newtonian gravitational force on a massless particle is zero. In terms of the effective potential, a photon with a given energy E will come in from $r = \infty$ and gradually "slow down" (actually $dr/d\lambda$ will decrease, but the speed of light isn't changing) until it reaches the turning point, when it will start moving away back to $r = \infty$. The lower values of L, for which the photon will come closer before it starts moving away, are simply those trajectories which are initially aimed closer to the gravitating body.

For massive particles there will be stable circular orbits at the radius r_c, as well as bound orbits which oscillate around this radius. If the energy is greater than the asymptotic value $E = 1$, the orbits will be unbound, describing a particle that approaches the star and then recedes.

The term of the potential, $-GML^2/r^3$, as $r \to \infty$ behaves in an analogous way to the Newtonian case.. But as $r \to 0$ the potential goes to $-\infty$ rather than $+\infty$ as in the Newtonian case. At $r = 2GM$ the potential is always zero; inside this radius is the black hole. For massless particles there is always a barrier (except for $L = 0$, for which the potential vanishes identically), but a sufficiently energetic photon will nevertheless go over the barrier and be dragged inexorably down to the center. At the top of the barrier there are unstable circular orbits. For $\epsilon = 0$, $\gamma = 1$, we can easily solve to obtain:

$$r_c = 3GM, \qquad (6)$$

For massive particles there are once again different regimes depending on the angular momentum. The circular orbits are at:

$$r_c = \frac{L^2 \pm \sqrt{L^4 - 12G^2M^2L^2}}{2GM}, (c = 1) \qquad (7)$$

For large L there will be two circular orbits, one stable and one unstable. In the $L \to \infty$ their radii are given by:

$$r_c = \frac{L^2 \pm L^2 \left(1 - 6G^2M^2/L^2\right)}{2GM}, \qquad (8)$$

In this limit the stable circular orbit becomes farther and farther away, while the unstable one approaches $3GM$. As we decrease L the two circular orbits come closer together; they coincide when the discriminant in Eq. (8) vanishes, at $L = \sqrt{12}GM$, for which $r_c = 6GM$ and disappear entirely for smaller L. $r_c = 6GM$ is the smallest possible radius of a stable circular orbit in the Schwarzschild metric. There are also unbound orbits, which come in from infinity and turn around, and bound but non-circular ones, which oscillate around the stable circular radius. Finally, there are orbits which come in from infinity and continue all the way in to $r = 0$; this can happen either if the energy is higher than the barrier, or for $L < \sqrt{12}GM$, when the barrier goes away entirely.

Therefore, the Schwarzschild solution possesses stable circular orbits for $r > 6GM$ and unstable circular orbits for $3GM$ (photon sphere's radius) $< r < 6GM$. But these are only the geodesics; there is nothing to stop an accelerating particle from dipping below $r = 3GM$ and emerging, as long as it stays beyond $r = 2GM$.

3.2 PyHole

PYHOLE is a ray tracing code written in Python 3 that can simulate the motion of light on the curved KBHSH background. It represents the motion of light rays that are emitted from a distant source and which eventually reach the position of an observer (or camera), perhaps having passed near the black hole along the way. In practice with PYHOLE light rays are traced backwards in time, starting at the camera, along null geodesics of the black hole metric. Each pixel on the camera image corresponds to a light ray with a different initial momentum vector, which will, as a result, follow a different trajectory; some rays will reach a distant light source, and some will not, having fallen instead behind the event horizon. The former will appear as bright pixels on the camera image and the latter as dark pixels. There is also a set of marginal trajectories

that enter into null orbits of the black hole and delimit the region of space that appears dark on the image plane, corresponding to the black hole's shadow.

PyHole uses the NumPy and SciPy extensions for scientic computing. This choice allows rapid and flexible design of the code and simple addition of features. Since Python is an interpreted language, the resulting code is platform independent and can be run on any system with a Python 3 interpreter. This flexibility comes at the cost of computational speed as Python code for numerical applications is typically slower than optimised native implementations in languages such as C++ or Fortran. However, by optimizing the code specifically for NumPy, modern Python implementations can reduce the overhead significantly.

3.3 Simulation results

In Fig. 1 there is a high resolution image of a Schwarzschild black hole shadow $(Q, L = 0)$ with Schwarzschild radius $R_s = 2$ (in geometric units), and impact parameter (in event horizon), $\eta = 5.1962$. We simulated some scenarios taking an observer distance of $r = 15$ to investigate the differences and compare. First, we examine the qualitative change of the image while gradually increasing R_s. Then, we analyze certain trajectories close to the shadow of the event horizon and look at the number of revolutions the photon has traveled around the black hole analyzing the winding number.

First, we qualitatively examine the difference of the shadow of an increasingly black hole. The images in Fig. 2 depict a Schwarzschild black hole with different values for R_s ($R_s = 2, 2.5, 3, 3.5$). As we can observe, the background isn't distorted. When increasing R_s, the coloured parts near the shadow of the event horizon keep undeformed. (see [21]). Now, examine the difference between the trajectories of orbits depending on the initial point. We choose three orbits from the upper left zone and three orbits from the lower right, some of them in the edge of the event horizon's shadow in the equatorial plane (see Fig. 3a). In the diagram in Fig. 3b we can clearly see that the trajectories with start at larger distances from the event horizon they pass further away than those at closer distance. This agrees with what was expected.

Next, we further explore certain geodesics close to the left side of the event horizon's shadow. For more simplicity we again restrict ourselves to trajectories in the equatorial plane. In Fig. 4a you can see a zoomed image in view of said left side of the event horizon's shadow. The numbers order the trajectories based on the simulation order which are shown in Fig. 3b. It is obvious that the closer you are to the black hole, the more often your trajectory winds around the black hole again. This exponentially increasing behaviour is also visible in Fig. 3b.

Let's analyze the Fig. 4c. As we can see, it's represented the winding num-

ber, which is the total number of times that the photon travels counterclockwise around the black hole, approximately. It's given by the quantity:

$$w = \frac{\phi}{2\pi},$$ (9)

As we can see, all the trajectories present negatives values between $-1.2 < w < 0$, which means that the photon spin around the black hole clockwise at most one time and there is at most one radial turning point in the orbits.

Finally, it can be argued that the major difference between the Kerr and Schwarzschild black holes is in how they are defined (a Kerr black hole rotates with an angular momentum which leads to them having different metrics, event horizon and an ergosphere radii, and singularities). However the Kerr black hole is a more generalized version of Schwarzschild black hole and due to $a = 0$, the simplification of the event horizon, ergosphere, singularity, and the Kerr to the Schwarzschild metric is not merely random. The Kerr and Schwarzschild black holes are not so different, despite the fact that there is no frame-dragging in this type of black hole (the rotating mass of the black hole causes frame-dragging) and the possibility of turn-back orbits which only appear in rotating black holes.
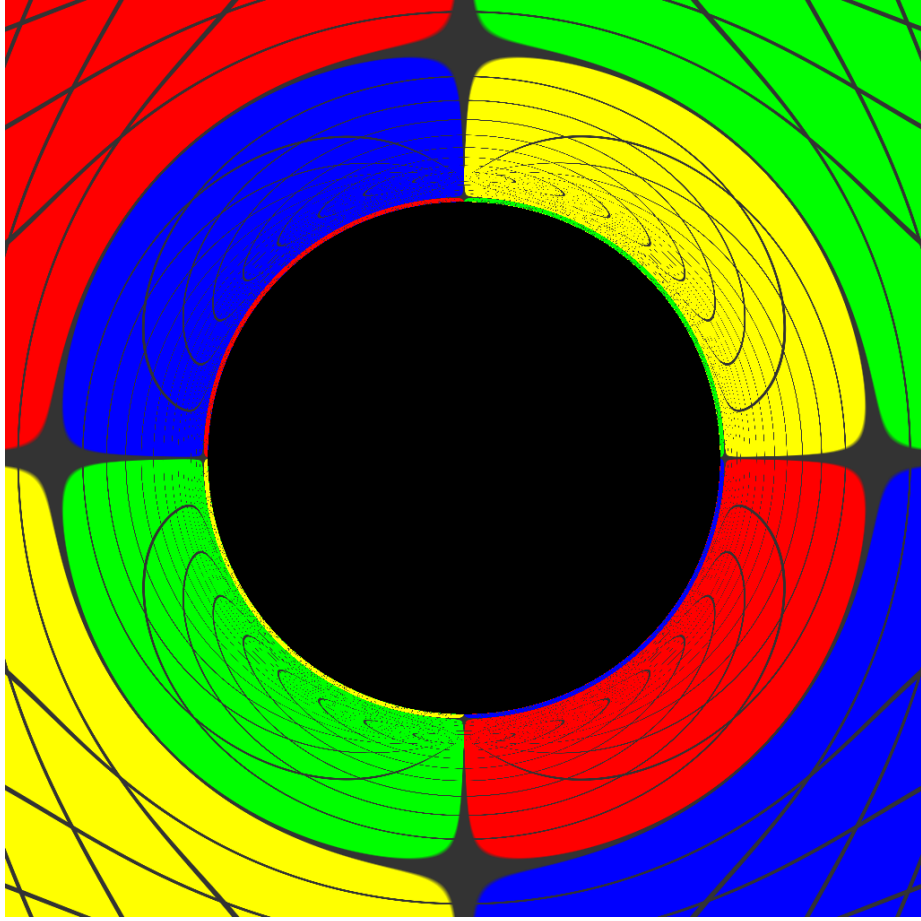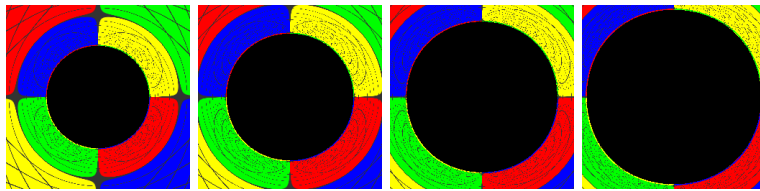
Figure 1: High resolution image of a shadow of Schwarzschild black hole generated using PyHole. Depicts the shadow of a non-rotating black hole with $R_s = 2$.

(a) $R_s = 2$ (b) $R_s = 2.5$ (c) $R_s = 3$ (d) $R_s = 3.5$

Figure 2: Four images of a shadow of a Schwarzschild black hole with different radius.

4 Kerr black holes

4.1 Theoretical background

4.1.1 Kerr metric

Another exact solution of the Einstein field equations is the Kerr solution. It describes a rotating, non-charged black hole. Therefore, the Kerr solution is an extension of the Schwarzschild solution with a non-zero angular momentum J. In geometrized units $G = c = 1$, using Boyer-Lindquist coordinates, the line element ds describing the Kerr metric is as follows

$$ds^2 = -\left(1 - \frac{R_s r}{\Sigma}\right) dt^2 + \frac{\Sigma}{\Delta} dr^2 + \Sigma\, d\theta^2 + \left(r^2 + a^2 + \frac{R_s r a^2}{\Sigma} \sin^2\theta\right) \sin^2\theta\, d\phi^2 - \frac{2R_s a r \sin^2\theta}{\Sigma} dt\, d\phi. \tag{10}$$

with

$$R_s = 2M, \quad a = \frac{J}{M}, \quad \Delta = r^2 - 2Mr + a^2, \quad \Sigma = r^2 + a^2 \cos^2\theta. \tag{11}$$

Here, r, θ, and ϕ denote the standard spherical coordinates. The metric describes a black hole at the origin $r = 0$ rotating in direction of the azimuthal, i.e., ϕ, coordinate. It is a stationary, axisymmetric metric. We use R_s to denote the Schwarzschild radius, i.e., the location of the event horizon of non-rotating black hole of mass equivalent M. Note that the Kerr metric for $a = 0$ is identical to the Schwarzschild metric in Eq. (1).

4.1.2 Horizons, static limit and ergosphere

A Kerr black hole has two horizons. Due to the coordinate singularity at $\Delta = 0$, Kerr spacetime exhibits two horizons at the radii $r_\pm = M \pm \sqrt{M^2 - a^2}$. Usually, only the larger radius r_+ is called *the horizon* of a Kerr black hole. In the non-rotating case $a = 0$, both radii $r_\pm$ coincide with R_s. Note that the horizons only take on real values if $a \leq M$. Therefore, if $a > M$, a naked singularity may be possible. Here, we restrict ourselves to values of $0 < a \leq M$.

The *static limit* is the area around the horizon of a black hole where it is impossible for any object to remain stationary. For a Schwarzschild black hole the static limit and the event horizon coincide. This, however, is not the case for rotating black holes. At distances less than $r_0 = M + \sqrt{M^2 - a^2 \cos^2\theta}$ from the black hole's center is it impossible to stand still. Due to frame dragging, every object must co-rotate with the black hole.

Note that $r_0 \geq r_+$. This implies that there exists a region between the of the border static limit and the horizon. This region is referred to as the *ergosphere*. Any object in the ergosphere has to co-rotate the black hole, but can still escape.
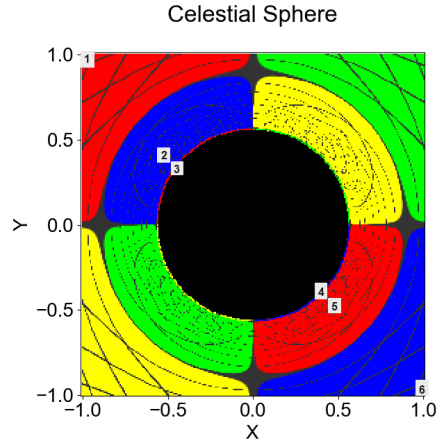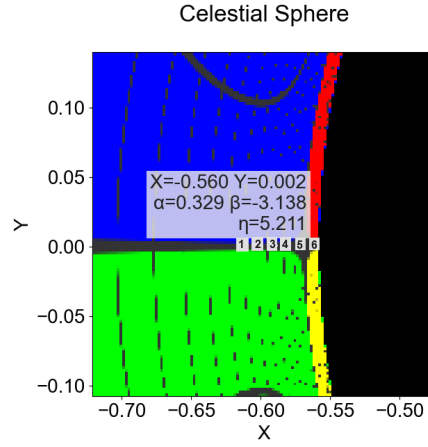
(a) Shadow of a non-rotating black hole.
The numbers indicate the location of the
projected origins of the trajectories shown
in Fig. 3b.
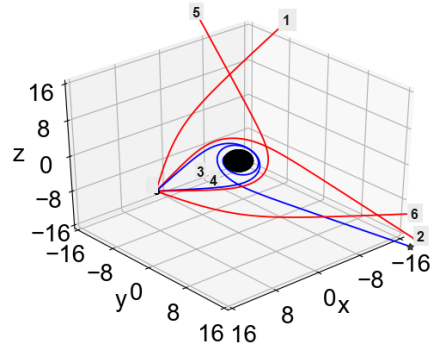
(b) Visualization of the trajectories. We can clearly
see that the closer you are to the black hole, the
more often your trajectory winds around the black
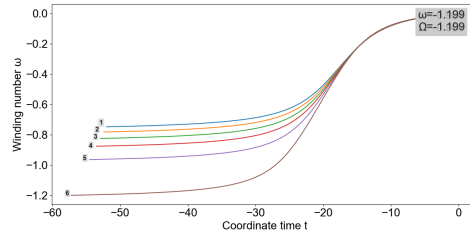hole again.

Figure 3: Visualization of six trajectories whose starting points are symmetri-
cally located.

Celestial Sphere

(a) Zoomed in view of the left side of the event horizon shadow. The numbers indicate the location of the projected origins of the trajectories shown in Fig. 4b and the value of the impact parameter, η
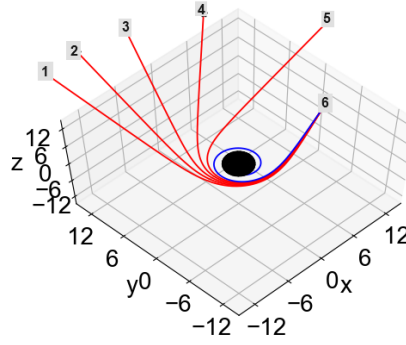
(b) Visualization of the trajectories again.

(c) Diagram of the winding numbers of the trajectories.

Figure 4: Visualization of six trajectories whose starting points are symmetrically located.

12

4.1.3 Photon trajectories and orbits

Due to the introduction of a rotational axis the Kerr metric no longer exhibits the spherical symmetry of the Schwarzschild metric. Rather, Kerr spacetime is axisymmetric about the rotational axis of the black hole. Therefore, generally, angular momentum is no longer conserved. Orbits can no longer be described as being contained to a single plane. These fully three-dimensional dynamics are laborious to analyze. As a consequence, we limit our analysis to the special case of equatorial orbits. Equatorial orbits lie fully within the equatorial plane $\theta = \pi/2$. This subset of all possible orbits is much simpler to discuss.

Moreover, we differentiate between *prograde* and *retrograde orbits*. Prograde orbits are orbits which revolve around the black hole in the same direction as the black hole's spin. Conversely, retrograde orbits orbit a black hole against the direction of its spin. Due to frame dragging prograde orbits can be thought of experiencing a pushing force. This allows them to orbit faster. Therefore, prograde orbits can exist much closer to the black hole. The inverse is true for retrograde orbits. Frame dragging slows these orbits down. This renders these orbits much farther away from the black hole. Furthermore, turn-around orbits, that is, orbits that change direction, are also only possible for retrograde orbits in Kerr spacetime.

4.2 Simulation results and discussion

The image in Fig. 5 shows a high resolution image of the shadow of a rotating black hole with $a = 0.5M$. We simulated a few scenarios to investigate several peculiarities of the shadows of such rotating black holes.

First, we examine the qualitative change of the simulated image of the shadow when gradually increasing the strength of the rotation. In particular, we analyze equatorial trajectories close to the shadow of the event horizon to study the number of revolutions the trajectory takes the black hole. Then, we compare trajectories that lie in the equatorial plane and those outside which lie outside of it. Further, we explore retrograde and prograde trajectories. And, finally, we inspect the possibility of turn-back trajectories.

4.2.1 Impact of rotational strength

First, we examine the differences in the images of the shadow of an increasingly rotating black hole qualitatively. The images in Fig. 6 depict a rotating black hole under the same circumstances but with different values for $a = 0.2M, 0.4M, 0.8M, 1.0M$. It is obvious that the background is increasingly distorted with higher rotational speeds. Due to frame dragging, the background gets twisted around the black hole in the direction of rotation. When increasing a, the green and blue parts near the shadow of the event horizon, which are
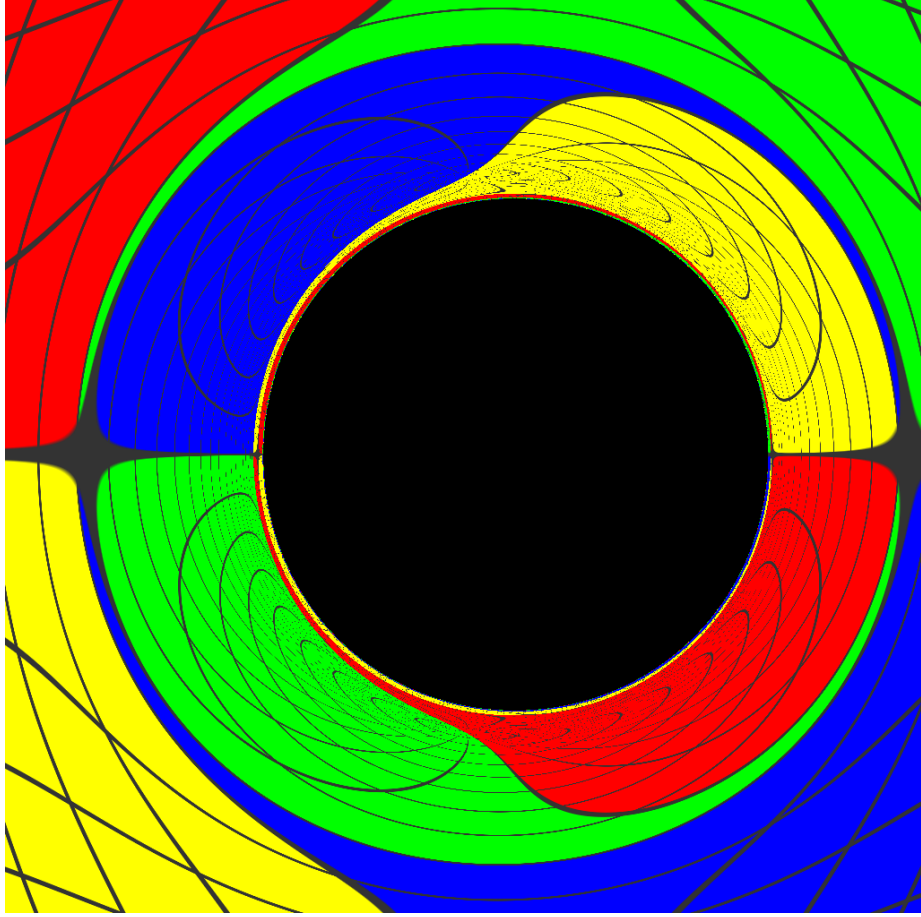
Figure 5: High resolution image of a shadow of Kerr black hole generated using PYHOLE. Depicts the shadow of a rotating black hole with $a = 0.5M$. The black hole rotates counter-clockwise, i.e., the left-hand side of the image is moving towards the observer.

(a) $a = 0.2M$ (b) $a = 0.4M$ (c) $a = 0.8M$ (d) $a = 1.0M$
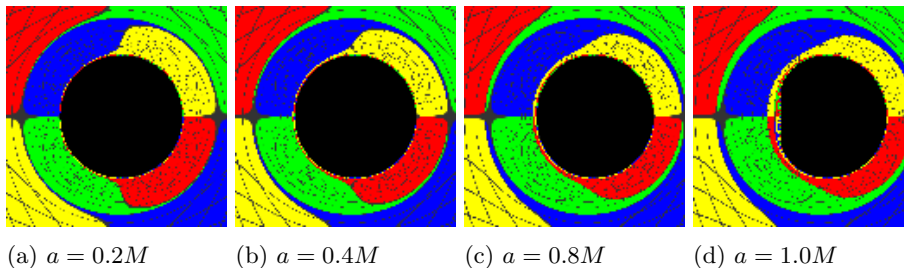
Figure 6: Four images of a shadow of a Kerr black hole with different angular momenta.

mainly on the left side, bleed into the right side of the image. Analogously, a similar effect happens with the yellow and red areas which are originally on the right side.

Another interesting effect happens near the shadow of the event horizon for large a, e.g. in Fig. 6d. Here, especially on the left side, you can see a wild, almost chaotic, mix of the four colors. This happens because the light trajectories revolve around the black hole multiple times. The closer to the black hole shadow, the more revolutions the trajectories may exhibit. This effect increases exponentially [18]. As the resolution of the images is not high enough, this behaviour cannot be resolved sufficiently. This leads to the apparent chaotic appearance.

4.2.2   Trajectory revolutions around the black hole

We further look into this behaviour by exploring certain prograde trajectories close to the left side of the event horizon's shadow. For the sake of simplicity we, again, restrict ourselves to trajectories in the equatorial plane. In Fig. 7a you can see a zoomed in view of said left side of the event horizon's shadow. The numbers label the apparent, projected origin of light rays whose actual trajectories are shown in Fig. 7b. It is obvious that the closer you are to the black hole, the more often your trajectory winds around the black hole. This exponentially increasing behaviour is also visible in Fig. 7a. Farther away from the black area you can almost make out the thin slivers of coherent colors before the resolution is not high enough and apparent chaos ensues. Finally, in Fig. 7c you can see the actual numbers of revolutions a trajectory takes around the black hole. Qualitatively, it is obvious that the winding number increases non-linearly with the decreasing distance from the black hole's center.

(a) Zoomed in view of the left side of the event horizon's shadow. The numbers indicate the location of the projected origins of the trajectories shown in Fig. 7b.

(b) Visualization of the trajectories (blue solid lines) around the rotating black hole (large black dot).

(c) Diagram of the winding numbers of said trajectories. The top-most graph corresponds to trajectory 1, the second-highest graph to trajectory 2, etc.
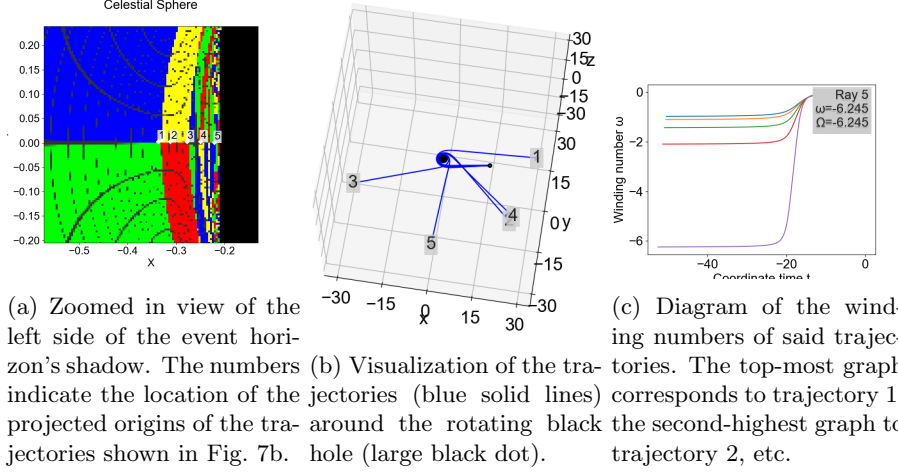
Figure 7: Three figures exploring the behaviour of prograde trajectories close to the event horizon's shadow. The closer you are to the black hole, the more often the trajectory winds around the black hole.
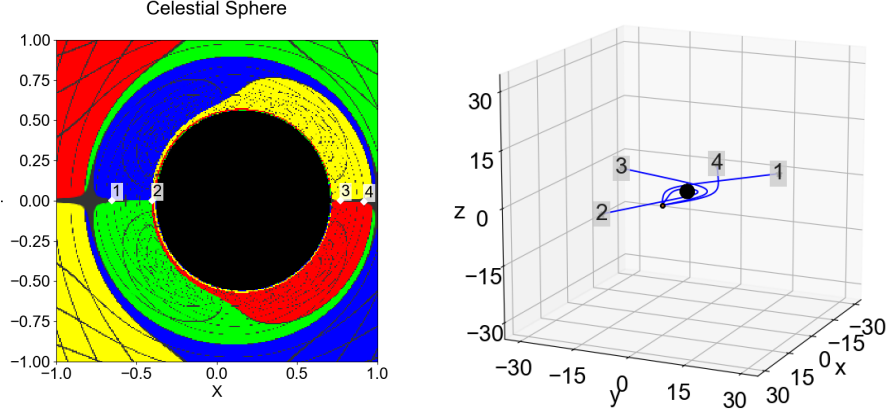
4.2.3 Non-equatorial trajectories

An important feature of rotating black holes are non-equatorial trajectories. These are trajectories which do not lie entirely in the equatorial plane. Such trajectories are not confined to a single orbital plane and, thus, exhibit complex fully three-dimensional dynamics.

In the images in Fig. 8 you can see a comparison of such equatorial (see Figs. 8a and 8b) and non-equatorial (see Figs. 8c and 8d) trajectories. You can clearly see that trajectories which lie in the equatorial plane also remain in it. Their trajectories are effectively two-dimensional like every trajectory in the spherically symmetric case. Trajectories which lie outside of the equatorial plane, however, exhibit more complex fully three-dimensional behaviour. It is obvious that their trajectories cannot be confined to a single two-dimensional plane.

4.2.4 Prograde and retrograde trajectories

We examine the prospected difference between prograde and retrograde trajectories. We choose three prograde trajectories and three retrograde trajectories close to the event horizon's shadow in the equatorial plane (see Fig. 9a). In the diagram in Fig. 9b you can clearly see that the prograde trajectories orbit the black hole at a closer distance than the retrograde trajectories. This matches with our expectation.

(a) Kerr black hole shadow with trajectories that lie in the equatorial plane $z = 0$.

(b) Visualization of the trajectories which remain fully in the equatorial plane.
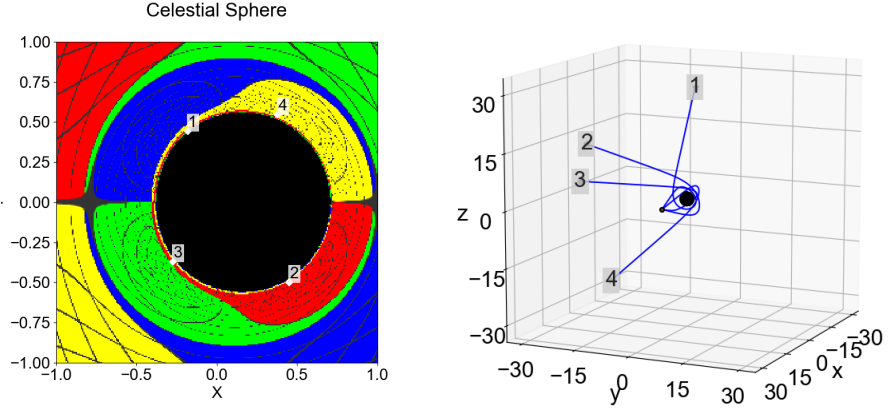
(c) Kerr black hole shadow with trajectories that lie outside of the equatorial plane $z = 0$.

(d) Visualization of the trajectories which freely roam outside of the equatorial plane.

Figure 8: The top two panels shows visualizations of trajectories which lie fully in the equatorial plane. In the bottom two panels such visualizations of non-equatorial trajectories can be seen. The left panels depict the shadow of the simulated rotating black hole ($a = 0.7M$). The numbered white diamonds show the location of the projected origins of the trajectories shown in the corresponding right panels. In the right panels you can see said trajectories (solid blue lines) around the rotating black hole (large black dot).

17
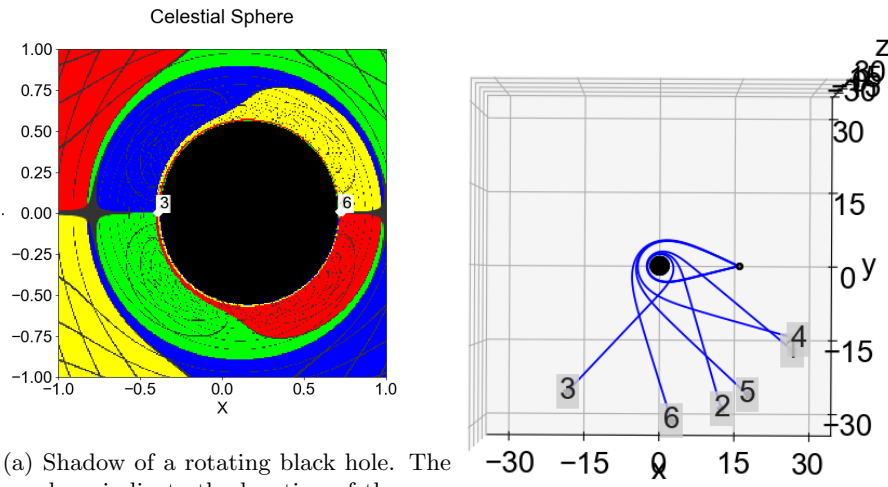
(a) Shadow of a rotating black hole. The numbers indicate the location of the projected origins of the trajectories shown in Fig. 9b. The labels 1 and 2 are hidden behind label 3 and approximately at the same location as label 3 but with a small variation in the x-direction. A analogous explanation holds for label 4 and 5 which are hidden behind label 6.

(b) Top-down view of a counter-clockwise rotating black hole (large black dot) with six trajectories (solid blue lines) of massless test particles. The prograde trajectories (labels 1-3) orbit the black at a systematically closer distance than the retrograde trajectories (labels 4-6).

Figure 9: Visualization of three prograde (1-3) and three retrograde (4-6) trajectories around a rotating black hole.
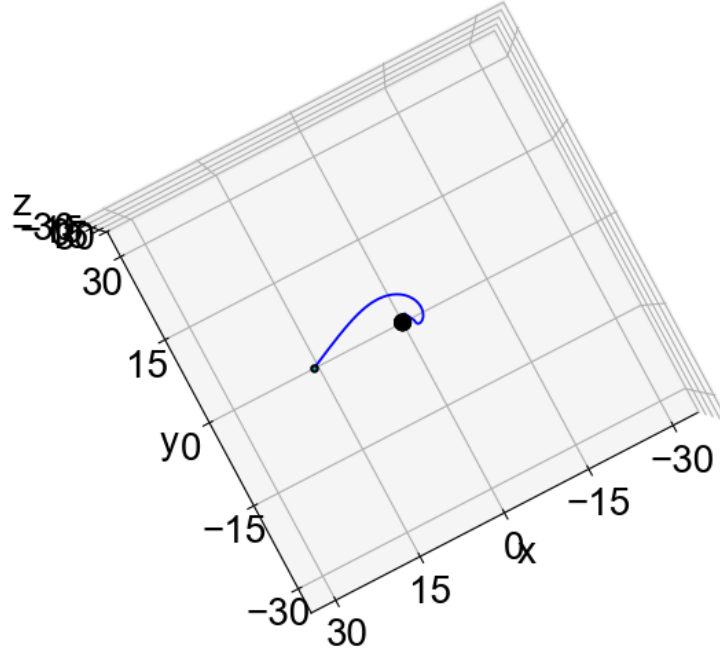
Figure 10: In this top-down view of a counter-clockwise rotating black hole (large black dot) you can see a visualization of a turn-back trajectory (solid blue line). The retrograde trajectory starts orbiting the black hole in a clockwise direction before turning around to orbit in the counter-clockwise direction and, finally, plummeting into the black hole.

4.2.5 Turn-back trajectories

Finally, we inspect the possibility of turn-back trajectories, which may only appear in rotating black holes.

In the image in Fig. 10 you can see such a trajectory. To find one, we simulated the shadow of a Kerr black hole with $a = 0.99M$. We investigated orbits in the equatorial plane that lie in the shadow of the event horizon. This retrograde trajectory changes its direction of rotation before plummeting into the black hole. Therefore we can classify it as a so-called turn-back trajectory.

5 Charged Black Holes

5.1 Introduction

A charged black hole is a black hole with an electric charge. A charged black hole may be rotating or non-rotating. A non-rotating charged black hole is described by the Reissner-Nordström metric, originally found by Reissner [15], whereas a rotating charged black hole is described by the Kerr-Newman metric [13]. This is the most general known kind of black hole metric (in classical general relativity) [23]. If we set the black hole's angular momentum to 0, we recover the Reissner-Nordström metric. If we set its charge to 0, we recover the Kerr metric. And, of course, if we set both to 0, we recover the Schwarzschild metric.

In practice, while charged black holes are expected to exist, their charge is expected to be so small that its effect will be completely negligible and they will be indistinguishable from Kerr black holes. Still, it is interesting to see what's the effect of charge on a black hole, so that we have a way to measure it and check if it's zero, as a check to see if black holes are formed the way we think they're formed.

For simplicity, let's begin by focusing on the case of a non-rotating charged black hole. Its metric, the Reissner-Nordström metric, is seen in equation 12, which can be found, for example, in [14] or [24]:

$$ds^2 = -\left(1 - \frac{r_S}{r} + \left(\frac{r_Q}{r}\right)^2\right)c^2 dt^2 + \left(1 - \frac{r_S}{r} + \left(\frac{r_Q}{r}\right)^2\right)^{-1} dr^2 \atop +r^2 d\theta^2 + r^2 \sin^2(\theta) d\phi^2 \tag{12}$$

Where r_S, r_Q are defined as stated in equations 13 and 14:

$$r_S = \frac{2GM}{c^2} \tag{13}$$

$$r_Q^2 = \frac{Q^2 G}{4\pi\varepsilon_0 c^4} \tag{14}$$

Note that r_S is the usual Schwarzschild radius. Thus, if the black hole is uncharged, $Q = 0$, then $r_Q = 0$ and the metric directly becomes the Schwarzschild metric. However, if the black hole is charged, $r_Q \neq 0$ and the metric is different from the Schwarzschild metric. Note that this means that even neutral particles will feel the effect of the charge via its effect on the metric, which is a purely relativistic effect.

Just like the Schwarzschild metric, this metric contains singularities, which can be found by seeing for which values of r the g_{rr} component will diverge. To

do that, one can set its inverse equal to 0 and solve for r. If one does that, one obtains the two solutions seen in equation 15:

$$r_{\pm} = \frac{1}{2}\left(r_s \pm \sqrt{r_S^2 - 4r_Q^2}\right) \tag{15}$$

Apart from that, there's still a singularity at $r = 0$, since the g_{tt} component diverges there. We see that, if $r_Q > r_S/2$, the argument of the square root in equation 15 becomes negative and thus g_{rr} never diverges, so there can be no event horizon and the singularity at $r = 0$ becomes a naked singularity. Therefore, black holes with $r_Q = r_S/2$ are called extremally charged black holes, and black holes with a higher charge are not expected to exist, or they would contain a naked singularity.

For this work, the photon sphere (i. e. the sphere where the unstable circular orbit for massless particles, such as photons, is situated) is of particular interest. Its radius can be calculated in a similar way as for a Schwarzschild black hole and can be found, for example, in [3] or [12], and is given by equation 16:

$$r_{ps} = \frac{1}{4}\left(3r_S + \sqrt{9r_S^2 - 32r_Q^2}\right) \tag{16}$$

We see that, for $r_Q = 0$, we recover the usual radius for the photon sphere of a Schwarzschild black hole, $r_{ps} = 3r_S/2$.

The reason why the photon sphere is relevant is that, for a spherically symmetric metric, the shadow that can be seen from afar is closely related to this photon sphere, since the most "internal" photons from the background that one can see are those that get infinitessimally close to the photon sphere - if they got closer than the photon sphere, they'd fall into the black hole instead.

More specifically, for a spherically symmetric metric written as in equation 17:

$$ds^2 = -A(r)dt^2 + B(r)dr^2 + C(r)d\Omega^2 \tag{17}$$

The formula for the size of the black hole shadow can be computed as in equation 18, taken from [20]:

$$r_{sh} = \sqrt{\frac{C(r)}{A(r)}}\Bigg|_{r_{ps}} \tag{18}$$

For the Ressiner-Nordström metric, we know $A(r)$, $B(r)$ and $C(r)$ from equation 12. Replacing (and taking $c = 1$), we get:

$$r_{sh} = \frac{r}{\sqrt{\left(1 - \frac{r_S}{r} + \left(\frac{r_Q}{r}\right)^2\right)}}\Bigg|_{r_{ps}} \tag{19}$$

Which can be rewritten as in equation 20:

$$r_{sh} = \frac{r_{ps}}{\sqrt{\left(1 - \frac{r_S}{r_{ps}} + \left(\frac{r_Q}{r_{ps}}\right)^2\right)}} \tag{20}$$

Where r_{ps} is the photon sphere radius given by equation 16. Together, equations 16 and 20 give us a theoretical prediction for the black hole shadow radius, which we can later check with our simulations.

5.2 Shadow of a charged black hole

Using PyHole, one can examine how the shadow of a charged black hole should look like by calculating the trajectories of photons around it. The main difficulty is that the Reissner-Nordström and the Kerr-Newman metric are not implemented in PyHole by default. However, it is possible to implement new metrics in PyHole, following the instructions on how to do that that are present in the tutorial. Following these instructions, I implemented the Reissner-Nordström metric. With the metric implemented, one can calculate the shadow of this metric. It is particularly interesting to compare it with the results for the Schwarzschild metric, to see what are the effects of the charge on gravity. Note that this is a purely relativistic effect - In Newtonian physics, gravity does not depend on the charge of the object that sources it, and thus any neutral particle (such as a photon, or even a neutrino) shouldn't be able to see this charge - But, if gravity itself depends on charge, this provides an indirect way for neutral particles to see this charge.

First of all, to check that the metric is correctly implemented, we can check that a Reissner black hole with $r_Q = 0$ is identical to a Schwarschild black hole (with the same Schwarzschild radius r_S) and thus they both yield identical shadows. The results are shown in the Fig. 11 and 12. We see that both figures are basically identical, suggesting that the metric was well implemented.

To investigate the effect of the charge on the black hole shadow, I also computed the shadows for the cases $r_Q = r_S/4$ and $r_Q = r_S/2$. This last case is the case of an extremally charged black hole: a higher charge is not expected to be possible, since it would lead to a naked singularity. We see the shadows of those two black holes in Fig. 13 and 14, respectively.

We see that all Reissner-Nordtröm black holes produce qualitatively similar shadows to a Schwarzschild black hole, since the Schwarzschild and Reissner-
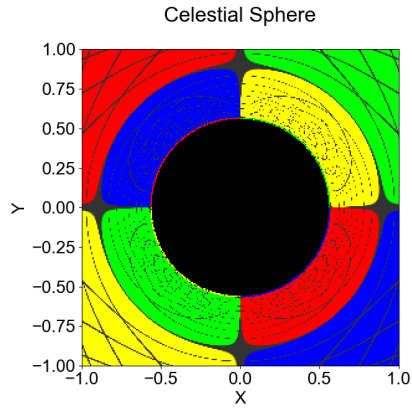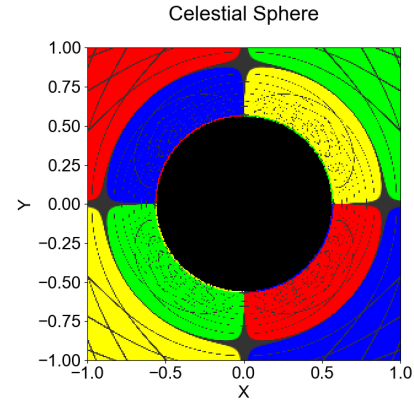
Figure 11: Schwarzschild Black Hole
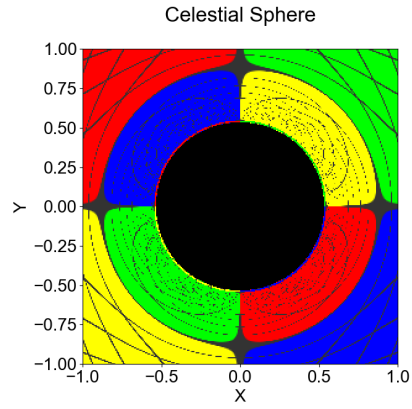

Figure 12: Reissner Black Hole with zero charge

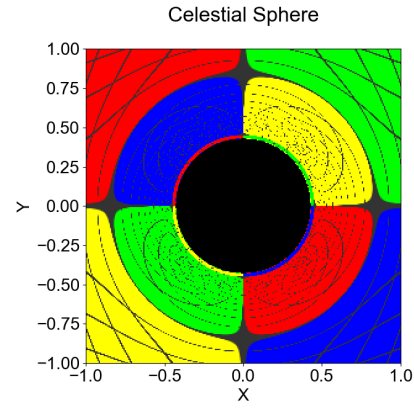Figure 13: Reissner Black Hole with $r_Q = r_S/4$

Figure 14: Reissner Black Hole with $r_Q = r_S/2$

Nordström metrics have a very similar mathematical structure. Most notably, both of them share the property of being spherically symmetric, which implies that black hole shadows must be rotationally symmetric for both of them, so we don't see the asymmetric effects that we'd see for a Kerr black hole, for example.

At the qualitative level, we see that the most notable difference between black hole shadows is that, at constant r_S, the size of the actual "black hole" that one sees in the image decreases as r_Q increases. This is not surprising: as stated in equation 15, we know that the horizon radius of a charged black hole decreases as its charge increases, and, even though we know that the radius of the actual black object we see in the image is not the event horizon radius, we know that the two radii are related.

In fact, we know that the radius of the black hole shadow is given by the theoretical prediction seen before (see equation 20).

From that equation, we can deduce that the ratio of the shadow radius of a charged black hole with respect to that of a neutral black hole with the same Schwarzschild radius is given by equation 21:

$$
x_{sh}(r_Q) \stackrel{\text{def}}{=} \frac{r_{sh}(r_Q)}{r_{sh}(r_Q = 0)} = \frac{r_{ps}(r_Q)\sqrt{\left(1 - \frac{r_S}{r_{ps}(r_Q=0)}\right)}}{\sqrt{\left(1 - \frac{r_S}{r_{ps}(r_Q)} + \left(\frac{r_Q}{r_{ps}(r_Q)}\right)^2\right)}r_{ps}(r_Q = 0)} \tag{21}
$$

Where $r_{ps}(r_Q)$ and $r_{ps}(r_Q = 0)$ can be obtained from equation 16.

This prediction allows us to make a quantitative test of our simulations. To do this, we measure the radius of the black hole seen in the image (in arbitrary units, but this doesn't matter because we're going to take ratios anyway). By measuring this radius, we're measuring the radius of the black hole shadow. We do this for several values of r_Q while keeping r_S constant, and, for each case, we divide by the value obtained for $r_Q = 0$ to obtain the corresponding ratio, which we can then compare to the ratio predicted by equation 21.

The results are shown in table 1.

The error of the measured value can be estimated by measuring the pixel size in our simulation in the coordinates x we're using. This pixel size is $\Delta x = 0.564 - 0.557 = 0.007$, and we can approximate the error for the measured distance as half the pixel size. We can then get an estimate of the error for the ratios by assuming both the numerator and the denominator have a relative error $(0.007/2)/0.557 \approx 0.006$, so the ratio has a relative error of approximately $\sqrt{2} \cdot 0.006 \approx 0.009 = 0.9\%$.

Thus, we see that the results in table 1 show that the predictions and the measurements are compatible with each other within the given measurement error, so, indeed, we have quantitative evidence supporting that our simulations

r_Q/r_S	$x_{sh}(r_Q)$: Prediction	$x_{sh}(r_Q)$: Measurement
0	1	1
0.125	0.989	0.986
0.25	0.956	0.957
0.375	0.893	0.887
0.5	0.770	0.774

Table 1: Comparison between the values for the ratio of shadow radii of charged black holes with respect to neutral black holes with the same mass as predicted by equation 21 and as measured in our simulations

are correct. We also see that the effect of the charge on the black hole shadow is relatively mild - even a maximally charged black hole has a shadow radius that's 77% as large as the shadow radius of a neutral black hole with the same mass.

Finally, we can ask ourselves how we can distinguish a charged black hole from a neutral one. We've already seen that the reduction in the shadow radius lets us distinguish a charged black hole from a neutral black hole with the same mass. However, a less massive neutral black hole might still have the same shadow radius, so... How do we tell the two cases apart?

One possibility is to determine the black hole's mass via an orbiting object. In the Reissner metric (equation 12), note that, for large r, the terms with $(r_Q/r)^2$ become negligible with respect to the terms with (r_S/r), so the effect of the charge on gravity becomes unnoticeable far from the black hole (which makes sense, since we expect to recover Newtonian gravity far from the black hole), so, if we see an object orbiting the black hole (and it's far away enough), we can use Newtonian physics to find the mass of the black hole it's orbiting - And, with the mass already known, measuring the shadow radius of the black hole can let us know its charge.

Another possibility, which doesn't require any other data than the event horizon image, is to look at other aspects of the image. Note, for example, that the outermost circle in the image (which marks the point where you start seeing light that was going in the opposite direction to the direction you're looking at before being bent by the black hole) doesn't get scaled down the same way as the shadow radius. For example, for a maximally charged black hole, as seen in table 1, the shadow radius decreases by a factor 0.77 with respect to a neutral black hole with the same mass. However, if we measure the radius of the outermost sphere, we see it's decreased by a factor 0.94 with respect to a neutral black hole with the same mass. We see the factor is closer to 1 (which makes sense, as we said, the effect of the charge on gravity decreases as the distance to the black hole increases). Since the two factors are different, the image isn't just the scaled down version of what we'd see for a Schwarzschild black hole, thus proving that the image cannot come from a less massive neutral

black hole and must come from a charged black hole.

6 Black hole mimicker

6.1 Theoretical background

We will focus on vacuum solutions of the Einstein equations, on the gravitational fields outside a static deformed body described by a parameter associated with the mass, m, and the deformation, γ. The latter tells us how far it departs from the Schwarzschild solution, coinciding for $\gamma = 1$.

The gamma-metric is an interesting model to study the behaviour of naked singularities [22], which is beyond the scope of the present work.

6.1.1 Gamma-metric

The gamma-metric is a static axially-symmetric vacuum solution of Einstein's equations belonging to Weyl's class that, in Erez-Rosen coordinates, is given by

$$ds^2 = -F\,dt^2 + F^{-1}[G\,dr^2 + H\,d\theta^2 + (r^2 - 2mr)\sin^2\theta\,d\phi^2], \qquad (22)$$

where

$$F(r) = \left(1 - \frac{2m}{r}\right)^{\gamma}, \qquad (23)$$

$$G(r,\theta) = \left(\frac{r^2 - 2mr}{r^2 - 2mr + m^2\sin^2\theta}\right)^{\gamma^2 - 1}, \qquad (24)$$

$$H(r,\theta) = \frac{(r^2 - 2mr)^{\gamma^2}}{(r^2 - 2mr + m^2\sin^2\theta)^{\gamma^2 - 1}}. \qquad (25)$$

This solution does not have an event horizon.

The dimensionless variable γ is known as the mass-density parameter, and describes how far the metric separates from the spherical symmetry. The total mass of the source is $M = \gamma m$ (the so-called gravitational mass).

We have different scenarios depending on γ:

- If $\gamma = 1$, a curvature singularity appears on the surface $r = 2m$, while in the Schwarzschild metric there was an event horizon. This singularity is independent of the value of θ, and it can not be avoid as in Schwarzschild by changing of coordinate system.

- If $\gamma \neq 1$, at $r = 2m = 2M/\gamma$, a true curvature singularity arises, which behaves, as in the Schwarzschild case, as an infinitely red-shifted surface.

That is, when $r \to 2m$, an observer at infinity will measure a frequency $\nu_\infty \to 0$. This observational property is analogous to an event horizon of a black hole for these observers at infinity. Such a curvature singularity is not covered by an event horizon, and it is like a prolate.

- If the value of γ takes negative values, one sees anti-gravitational effects associated with negative masses, which we will not go into here. One can also think of the possibility that quantum effects can be important near the surface $r = 2m$ for any value of γ, affecting the structure of the horizon, while for $r > 2M$ we recover the classical solutions, which we will not go into further.

If we were able to measure the coefficients of this metric in the neighbourhood of $r = 2m$, we could distinguish this metric from the Kerr metric, for example, which is currently beyond our reach.

Following the literature, $1/2 \leq \gamma \leq 1$ are solutions that do not differ much from the Schwarzschild solutions. In this interval, as the photon approaches the capture surface, the deflection angle increases. Such an interval they may act like Kerr black holes in that it produces analogous shadows.

6.1.2 Singularities

We can calculate the invariant scalars to see the behaviour of the singularities. Since we are in a vacuum solution, the Ricci scalar vanishes, but the Kretschmann scalar does not, which depends on the Riemannian curvature tensor $R_{\alpha\beta\delta\lambda}$, such that:

$$\kappa = R_{\alpha\beta\delta\lambda}R^{\alpha\beta\delta\lambda} = \frac{16m^2\gamma^2 N(r,\theta)}{r^{2(\gamma^2+\gamma+1)}(r-2m)^{2(\gamma^2-\gamma+1)}(r^2-2mr+m^2sin^2\theta)^{3-2\gamma^2}},$$
(26)

where

$$N(r,\theta) = m^2 sin^2\theta[3m\gamma(\gamma^2+1)(m-r)+\gamma^2(4m^2-6mr+3r^2)+m^2(\gamma^4+1)]+3r(\gamma m+m-r)^2(r-2m).$$
(27)

The Kretschmann scalar diverges for $r = 0$, for all $\gamma > 0$ (range of interest). Particularly for $\theta = 0, \pi, \pi/2$, the scalar will take the following values:

$$\kappa|_{\theta=0} = \kappa|_{\theta=\pi} = \frac{48m^2\gamma^2(\gamma m + m - r)^2}{r^{4+2\gamma}(r - 2m)^{4-2\gamma}},$$
(28)

$$\kappa|_{\theta=\pi/2} = \frac{16m^2\gamma^2 I(r)}{r^{2\gamma^2+2\gamma+2}(r - 2m)^{2\gamma^2-2\gamma+2}(r - m)^{6-4\gamma^2}},$$
(29)

where

$$I(r) = m^4(\gamma^4+3\gamma^3+4\gamma^2+3\gamma+1)-3m^3r(\gamma^3+4\gamma^2+5\gamma+2)+3m^2r^2(2\gamma^2+6\gamma+5)-6mr^2(\gamma+2)+3r^4.$$
(30)

27

We see then that for $\gamma < 2$, this scalar diverges for $r = 2m$ in the interval $\pi/2 \geq \theta \geq 0$, whenever it is not $=0$ (flat Minkowski) or $=1$ (Schwarzschild), while for $\gamma > 2$ it only diverges for $\theta = \pi/2$, being in this last case a directional singularity.

According to equation 26, we have another singularity for $r^2 - 2mr + m^2 \sin^2 \theta = 0$, provided that $\sqrt{3/2} \geq \gamma > 0$, associated to another singularity inside the surface $r = 2m$, so it will not affect us.

For M87, if we restrict the tilt angle to $\theta = 17°$, the jet axis and the line of sight would coincide, and the shadow size would be consistent for $1 \geq \gamma \geq 1/2$ [17].

We will take $M = 1$ because the mass only changes the size without affecting the shape of the shadow.

6.1.3   Metric and derivatives for code

Then, the components of our metric will be the following. First, for $g^{tt} = -F^{-1}$, its derivative is:

$$\partial_r g^{tt} = -g^{tt}\gamma \left(1 - \frac{2m}{r}\right)^{-1} \frac{2m}{r^2} \tag{31}$$

Secondly, for $g^{rr} = FG^{-1}$, its derivatives are:

$$\partial_r g^{rr} = \frac{2FG^{-1}}{r(r - 2m)}\left[m\gamma + (\gamma^2 - 1)\frac{(r - m)m^2 sin^2\theta}{r^2 - 2mr + m^2 sin^2\theta}\right]. \tag{32}$$

and

$$\partial_\theta g^{rr} = \frac{FG^{-1}(\gamma^2 - 1)2m^2 sin\theta cos\theta}{r^2 - 2mr + m^2 sin^2\theta}. \tag{33}$$

Thirdly, for $g^{\theta\theta} = FH^{-1}$, its derivatives are:

$$\partial_r g^{\theta\theta} = 2FH^{-1}\left[\frac{m\gamma(1 - 2m/r)^{-1}}{r^2} + (r - m)\left(\frac{\gamma^2 - 1}{r^2 - 2mr + m^2 sin^2\theta} - \frac{\gamma^2}{r^2 - 2mr}\right)\right] \tag{34}$$

and

$$\partial_\theta g^{\theta\theta} = 2m^2 FH^{-1}\frac{(\gamma^2 - 1)sin\theta cos\theta}{r^2 - 2mr + m^2 sin^2\theta}. \tag{35}$$

Finally, for $g^{\phi\phi} = F/((r^2 - 2mr)sin^2\theta)$, its derivatives are:

$$\partial_r g^{\phi\phi} = 2F\frac{m\gamma - r + m}{(r^2 - 2mr)^2 sin^2\theta} \tag{36}$$

and

$$\partial_\theta g^{\phi\phi} = -\frac{2Fcos\theta}{(r^2 - 2mr)sin^3\theta}. \tag{37}$$

6.1.4 Trajectories

We will now focus on the photon trajectories in the presence of the potential [1].

To study the motion of photons in this metric, we will assume that there are two constants of motion along the null geodesics: the energy $E = -p_t$ and the angular momentum $L = p_\phi$, associated with the equations of the geodesics:

$$\dot{t} = -E/g_{tt}, \tag{38}$$

$$\dot{\phi} = L_z/g_{\phi\phi}, \tag{39}$$

where the derivatives are with respect to the proper time of the particle. From the condition for the photons for the 4-velocity $u^\mu u_\mu = 0$ through the null geodesics, we obtain:

$$-g_{tt}(g_{rr}\dot{r}^2 + g_{\theta\theta}\dot{\theta}^2) + \frac{-g_{tt}}{g_{\phi\phi}}L^2 = E^2, \tag{40}$$

such that, by analogy, the effective photon potential will be:

$$V_{eff} = \frac{L^2}{r^2 sin^2\theta}\left(1 - \frac{2m}{r}\right)^{2\gamma-1}. \tag{41}$$

The photon capture is calculated for the minimum of the potential, and corresponds for:

$$r_{ps} = (2\gamma + 1)m = 2M + \frac{M}{\gamma}. \tag{42}$$

Such a capture will be possible as long as $\gamma \geq 1/2$ since then $r_{ps} \geq 2m$, so if any photon enters this surface, it will be captured by the singularity. Note that this is consistent with $\gamma = 0$, which corresponds to Minkowski, where the photon capture will be at infinity.

6.2 Simulation results

We will do all the results for the gamma-metric for an object of $M = 1$, unit mass, since what interests us is the study of the shape of the shadow, which is independent of the mass.

Let's start by explaining what happens if we put a value of $\gamma = 0.2$, see Fig. 15. This image is quite different from the Schwarzschild solution, see Fig. 16, where we have the case $\gamma = 1$, but as we said, in this limit is identical to Schwarzschild in the practical case. The only difference is in the potential, which, due to the internal singularity that appears in this metric, see Fig. 17. If the photon managed to enter inside the red arrow, which indicates the position closest to the centre of the object where the unstable orbit occurs, it would
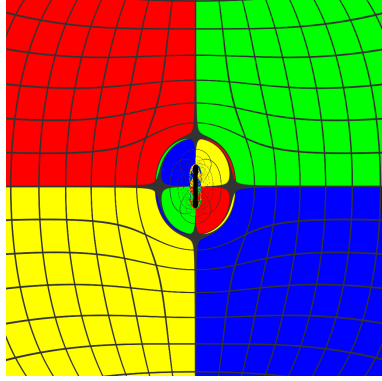
29

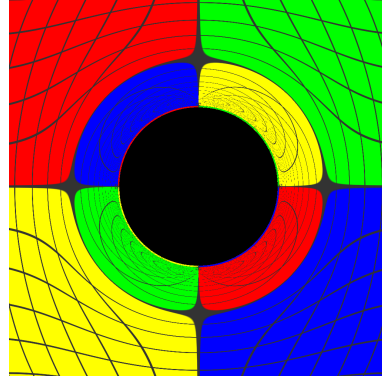Figure 15: Shadow Gamma-metric for Figure 16: Gamma-metric for $\gamma = 1$ and $\gamma = 0.2$ and $\theta = \pi/2$. $\theta = \pi/2$.
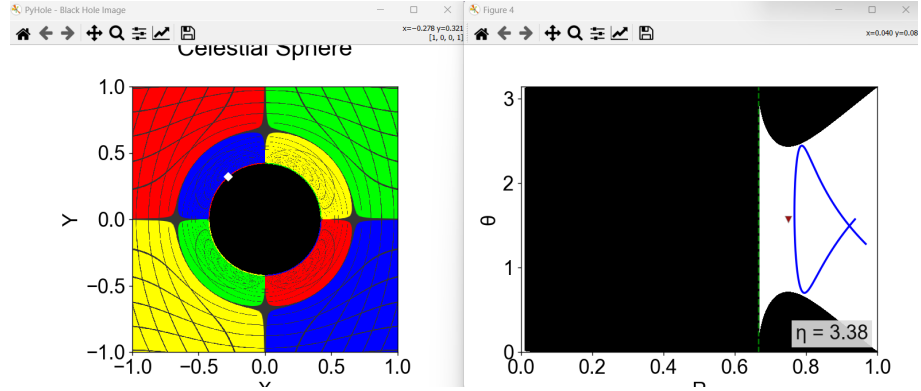

Figure 17: Gamma-metric shadow for $\gamma = 1$ and $\theta = \pi/2$, and the potential as a function of the angle and the distance for the photon with an impact parameter of $\eta = 3.38$.
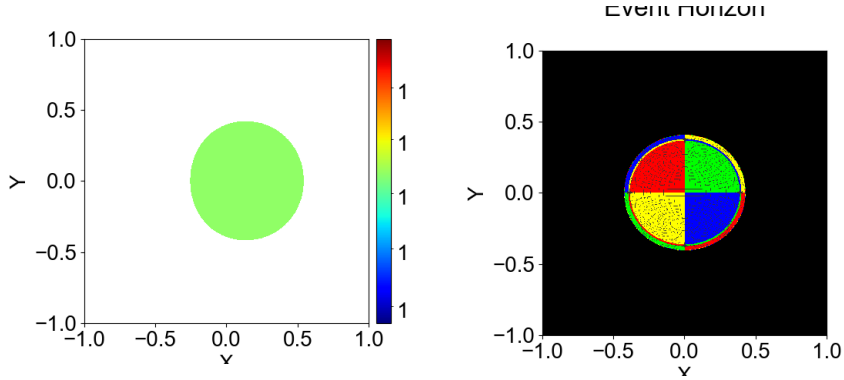
Figure 18: Shadow segmentation of a Kerr black hole for $a = 0.8$ and $\theta = \pi/2$.

Figure 19: Gamma-metric event horizon for $\gamma = 1.5$ and $\theta = \pi/2$.
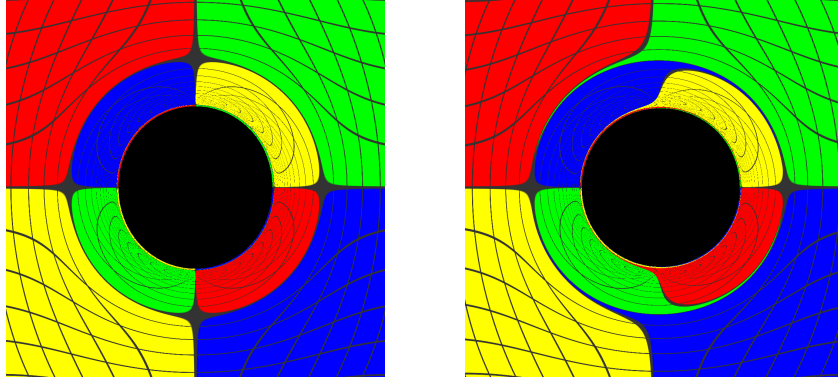

Figure 20: Gamma-metric for $\gamma = 0.81$ and $\theta = \pi/2$.

Figure 21: Kerr black hole shadow for $a = 0.2$ and $M = 2$.

touch the black surface and disappear. This is not seen in Schwarzschild since where it was an event horizon: here, this surface correspond with the curvature singularity. Nevertheless, both effects rise to analogous results in practice.

Then, we need larger values of γ. We will take into account that Kerr deforms as a prolate object when rotating very fast and not as an oblate, as it looks at Fig. 18. If we take an excessively high value of γ, such as $\gamma = 1.5$, we can see at Fig. 19 that its event horizon takes the form of an oblate. We can therefore rule out solutions with $\gamma > 1$ as candidates for black holes mimickers.

Let's take the case where $\gamma = 0.81$ and $\theta = \pi/2$, see Fig. 20. Indeed, it now takes on a more elongated shape at the poles, and in that respect is more analogous to a Kerr black hole. The difference is the rotation that Kerr can present in relation to the objects presented here, clearly reflected in the shadow and background. That is, for Kerr with $a = 0.2$, see Fig. 21, there is a
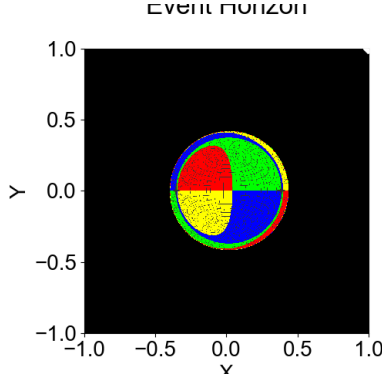
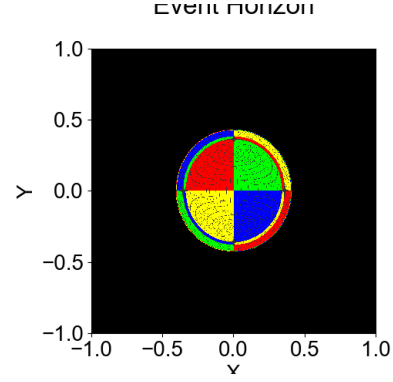Figure 22: Event horizon for Kerr black hole with $a = 0.1$.

Figure 23: Event horizon for gamma-metric with $\gamma = 0.81$ and $\theta = \pi/2$.
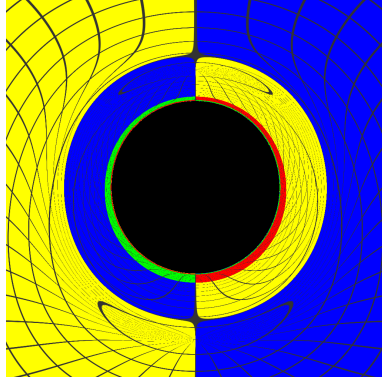

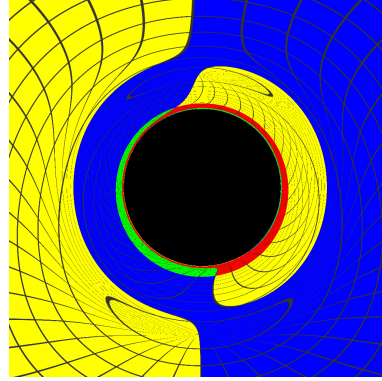Figure 24: Gamma-metric shadow for $\gamma = 0.5$ and $\theta = 17^{\text{o}}$.

Figure 25: Kerr black hole shadow for $a = 0.4$ and $\theta = 17^{\text{o}}$.

clear difference between the two shadows, with the Kerr background being quite distorted compared to the gamma-metric. This indicates that the gamma-metric will be a good mimicker as long as the astronomical object under study does not have a high rotation, otherwise the optical effects would be too different.

Taking a Kerr black hole with $a = 0.1$, it is a little more similar to Schwarzschild, but it is still different, especially if we compare their event horizons, see Fig. 22 and 23, where a clear difference is seen despite the small rotation of the black hole.

If we observe the object at an angle of 17°, according to the gamma-metric for $\gamma = 0.5$ we would have what we see at Fig. 24, which can be compared to what would be observed for a Kerr black hole at the same angle in Fig. 25. Big differences are seen again.

However, it should be noted in our favour that supermassive black holes at

the centre of the Milky Way are studied for $SagA*$, with a mass of the order of $10^6 M_\odot$. Since Kerr black holes depend on $a = J/M$, if the mass value is very high, it would be realistic to think that this value could be $a \ll 1$, always if it is fulfilled that $J \ll M$.

Then, the gamma-metric is a good mimicker for the case where $a \ll 1$.

7 Event Horizon Telescope

7.1 Introduction

The Event Horizon Telescope (EHT) [1] is an international collaboration that has formed to improving the capability of Very Long Baseline Interferometry (VLBI) at short wavelengths to directly observe the immediate environment of a black hole with angular resolution comparable to the event horizon. It has been used to measure the size of the emission regions of the two supermassive black holes:

- SgrA* at the center of the Milky Way.

- M87* in the center of the Virgo A galaxy.

M87 is a giant elliptical galaxy in the constellation Virgo a 50 million light years from Earth. M87 harbors a supermassive black hole living at its center. This black hole is one of the most massive known, 6 billion times more massive than our Sun. The most striking feature of M87 is a narrow, one-sided jet emanating from its center and extending for thousands of light years.

In 2019 the EHT Collaboration (EHT) published the first real image of a black hole [5, 6], (Fig. 26) of the supermassive black hole M87* at 1.3 mm wavelength with an unprecedented high angular resolution:

- Consistent with the shadow of a Kerr black hole of general relativity.

- Asymmetric bright emission ring with a diameter of 42 ± 3 μas.

- Mass for the M87* black hole of $(6.5 \pm 0.7) \times 10^9$ $M_\odot$.

- The analysis of the accretion disk suggest that the specific spin parameter a/M lies in the range from 0.5 to 0.94.

7.2 Simulation of M87* shadow shape as a Kerr black hole

A black hole without surrounding matter appears as a perfectly black patch in the sky of an observer, the so-called black hole shadow. With the shadow of

---

[1] https://eventhorizontelescope.org/

Figure 26: First image of a black hole, using Event Horizon Telescope observations of the center of the galaxy M87. Credit: Event Horizon Telescope Collaboration

M87* and Sagittarius A* clearly visible in the image and the prospect of future black hole images, the study of black hole shadows is now more relevant than ever.

We consider in our simulation a radius of $R = 2M$ and a distant observer with $r = 15M$ in geometric units. The existence of an horizon is proof of the presence of a black hole. Fig. 27 shows the simulation of a flat space, a Schwarzchild black hole and a Kerr black hole with the rotation parameter and observation angle estimated for M87*. It is observed that in a flat space there is no shadow, in a Schwarzschild black hole the shadow is perfectly circular and in a Kerr black hole a shadow is observed with the center displaced, a smaller area than that of Schwarzschild and with a slight distortion.

(a) Flat Space   (b) Schwarzschild black hole   (c) Kerr black hole
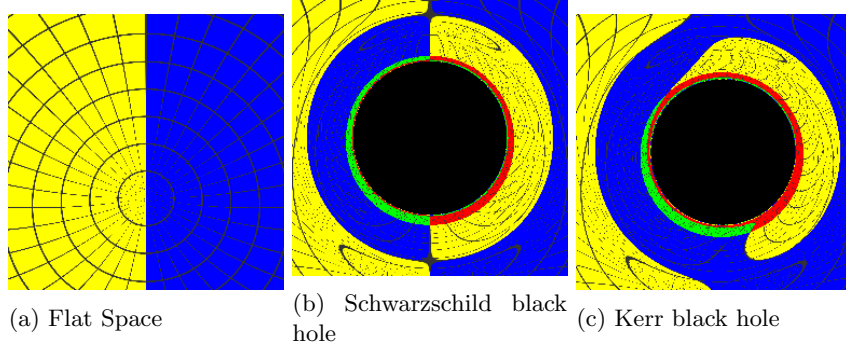
Figure 27: Simulation

We use PyHole to simulate the shadow of a Kerr black hole with the parameters of rotation [19] and observation angle estimated for M87*:

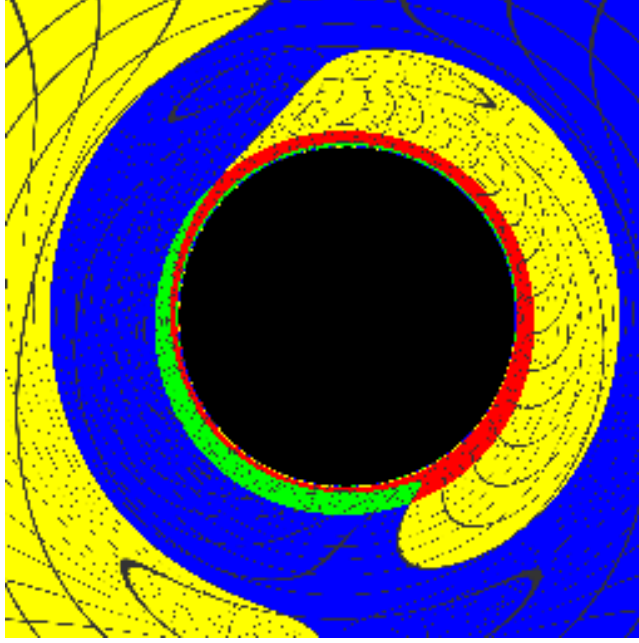- $a = 0.90\,M$ (0.90 ± 0.05).
- $\theta = 17°$ $(17° \pm 2°)$.

34

Figure 28: M87* shadow shape simulation $a = 0.9$, $\theta = 17°$

The simulation results (Fig. 28) show an off-center displacement of the shadow along the direction of black hole rotation (DC = 0.52) and a figure very close to a circle as expected (Oblateness D = 0.99).

7.3   Black hole shape parameter estimation from its shadow

A natural question to ask is whether the image of a shadow can be used to determine properties of the black hole such as the spin parameter a of a Kerr black hole. As seen in the Fig. 29 a non rotating black hole casts a perfectly circular shadow. However, for a rotating black hole, an observer placed at a position other than in the polar directions witnesses an off-center displacement of the shadow along the direction of black hole rotation. Furthermore, for sufficiently large values of the spin parameter, a distortion appears in the shadow because of the Lense-Thirring effect.

Hioki and Maeda [9] characterized this distortion and shadow size by the two observables δs and Rs, respectively. The shadow is approximated to a circle passing through three points located at the top, bottom, and right edges of the shadow, such that Rs is the radius of this circle and δs is the deviation of the left edge of the shadow from the circle boundary.

Kumar and Ghosh [11] consider more general observables: the area (A) enclosed by a black hole shadow, the circumference of the shadow (C), and

(a) Schwarzschild black hole

(b) Kerr black hole with $a = 0.90$
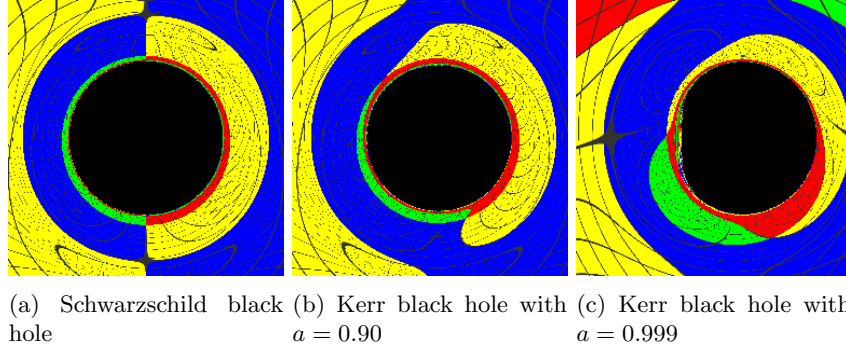
(c) Kerr black hole with $a = 0.999$

Figure 29: Changes in the shape of the black hole shadow

the oblateness (D) of the shadow (Kerr shadow $\sqrt{3}/2 \leq D < 1$). It can be expected that an observer targeting the black hole shadow through astronomical observations can measure the area, the length of the shadow boundary, and also the horizontal and vertical diameters.

We simulate (Kerr black hole, $\theta = 17°$, $R = 2M$, $r = 15M$)) for various spin parameter and calculate the A (area), C(circumference) and D (oblateness) parameter. In Fig. 30 we show the results of the simulation with PyHole and in table 2 we show the values of the observables A, C, and D.

A (pixels)	D	C/M	a/M
16004	1.000	31.03	0.00
15973	1.000	31.00	0.10
15812	0.993	30.85	0.30
15510	1.000	30.54	0.50
15016	1.000	30.05	0.70
14261	0.993	29.28	0.90
13732	0.992	28.75	0.999

Table 2: Area, Circumference and Oblateness of the black hole shadow

Next we simulate (Kerr black hole, $a = 0.9$, $R = 2M$, $r = 15M$)) for various observation angle parameter and calculate the A (area), C(circumference) and D (oblateness) parameter. In Fig. 31 we show the results of the simulation with PyHole and in table 3 we show the values of the observables A, C, and D.

Fig. 32 shows the dependence between the observables and the spin and observation angle parameters for a Kerr black hole.

Kumar and Ghosh [11] calculate the shadow observables and angular diameters of M87* black hole shadows for various values of spin parameter a. Results for M87* black hole are consistent with existing results. Comparing the the-

(a) $a = 0.1$ (b) $a = 0.3$ (c) $a = 0.5$

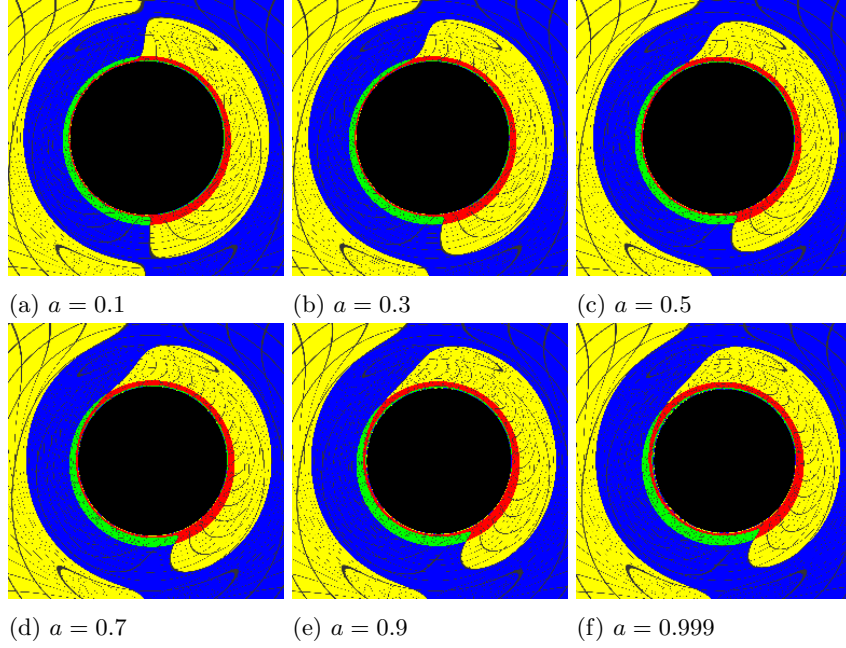(d) $a = 0.7$ (e) $a = 0.9$ (f) $a = 0.999$

Figure 30: Simulation of a Kerr black hole shadow for various spin parameters

oretically calculated values of these observables with those obtained from the astrophysical observations, it is expected that one can completely determine information about a black hole.

Characterizing the shadow of a black hole using observables has the potential to determine the value of the characteristic parameters of the black hole model that best fits the observations.

8   Conclusion

After all the work, where we have studied in depth the different kind of black holes, seeing how they affect the background, and their event horizon, we can conclude that the shadow of M87* seems to be well described by the Kerr metric. In the future, more data will be extracted from the black hole, and it will be more evidence for this conclusion.
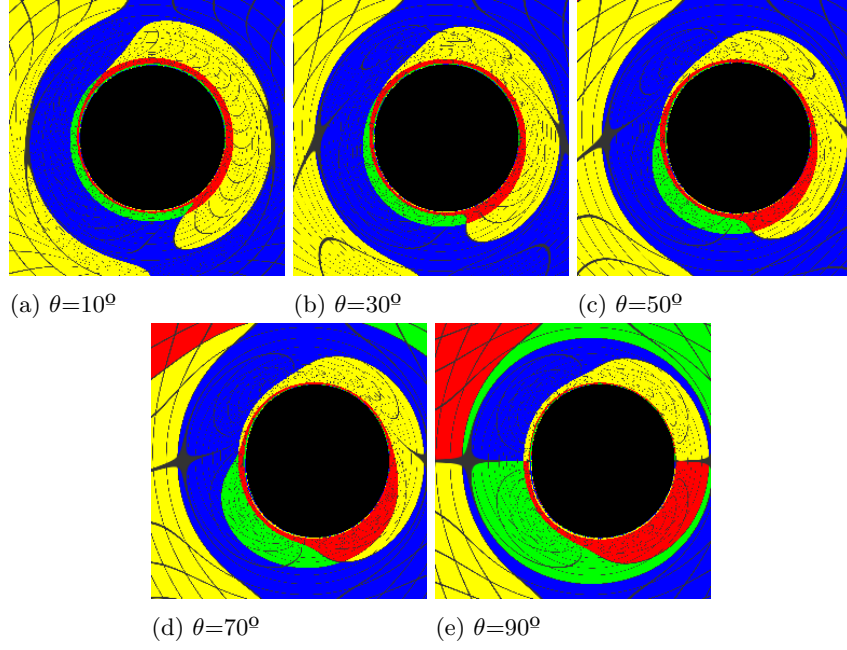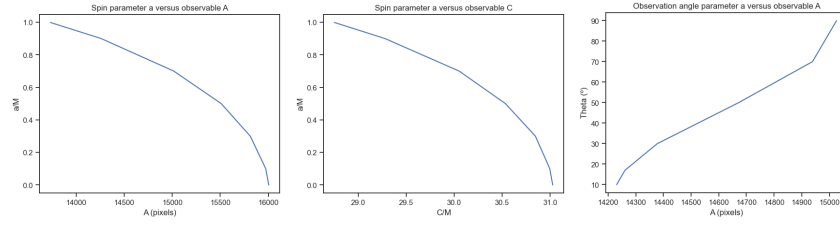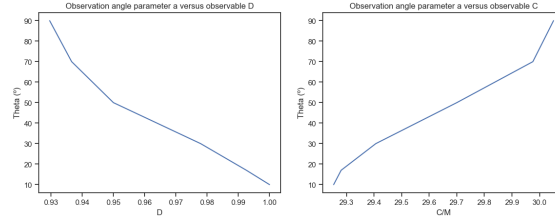
(a) $\theta=10^{\text{o}}$ (b) $\theta=30^{\text{o}}$ (c) $\theta=50^{\text{o}}$

(d) $\theta=70^{\text{o}}$ (e) $\theta=90^{\text{o}}$

Figure 31: Simulation of a Kerr black hole shadow for various angle of observation

A (Pixels)	D	C/M	θ ($^{\text{o}}$)
14231	0.930	30.05	10.00
14378	0.937	29.98	30.00
14672	0.950	29.70	50.00
14939	0.978	29.41	70.00
15026	1.000	29.25	90.00

Table 3: Area, Circumference and Oblateness of the Black Hole Shadow

(a) Spin parameter vs A (b) Spin parameter vs C (c) Angle vs A

(d) Angle vs D   (e) Angle vs C

Figure 32: Dependence between the observables and the spin and observation angle parameters

References

[1] Abdikamalov, Askar B. ; Abdujabbarov, Ahmadjon A. ; Ayzenberg, Dimitry ; Malafarina, Daniele ; Bambi, Cosimo ; Ahmedov, Bobomurat: Black hole mimicker hiding in the shadow: Optical properties of the γ metric. In: *Physical Review D* 100 (2019), Nr. 2, S. 024014

[2] Carroll, S.: *Lecture notes on General relativity: The Schwarzschild solution and black holes.* – URL https://ned.ipac.caltech.edu/level5/March01/Carroll3/Carroll7.html

[3] Claudel, Clarissa-Marie ; Virbhadra, K. S. ; Ellis, G. F. R.: The geometry of photon surfaces. In: *Journal of Mathematical Physics* (2000)

[4] Collaboration, Event Horizon T. u. a.: First Sagittarius A* Event Horizon Telescope results. I. The shadow of the supermassive black hole in the center of the Milky Way. In: *arXiv preprint arXiv:2311.08680* (2023)

[5] Collaboration, The Event Horizon T.: First M87 Event Horizon Telescope Results. I. The Shadow of the Supermassive Black Hole. In: *The Astrophysical Journal Letters* 875 (2019), apr, Nr. 1, S. L1. – URL https://dx.doi.org/10.3847/2041-8213/ab0ec7

[6] Collaboration, The Event Horizon T.: First M87 Event Horizon Telescope Results. VI. The Shadow and Mass of the Central Black Hole. In: *The Astrophysical Journal Letters* 875 (2019), apr, Nr. 1, S. L6. – URL https://dx.doi.org/10.3847/2041-8213/ab1141

[7] Deser, S. ; Franklin., J.: De/re-constructing the Kerr Metric. In: *General Relativity and Gravitation* (2010). – URL https://arxiv.org/abs/1002.1066

[8] Guerrero, Merce ; Olmo, Gonzalo ; Rubiera-Garcia, Diego ; Gómez, Diego: Shadows and optical appearance of black bounces illuminated by a thin accretion disk. In: *Journal of Cosmology and Astroparticle Physics* 2021 (2021), 08, S. 036

[9] Hioki, Kenta ; Maeda, Kei-ichi: Measurement of the Kerr spin parameter by observation of a compact object's shadow. In: *Phys. Rev. D* 80 (2009), Jul, S. 024042. – URL https://link.aps.org/doi/10.1103/PhysRevD.80.024042

[10] Hughes, Scott A.: *Introduction to relativity and spacetime physics: Lecture 21: Data on strong gravity.* 2021. – URL https://web.mit.edu/sahughes/www/8.033/lec21.pdf

[11] Kumar, Rahul ; Ghosh, Sushant G.: Black Hole Parameter Estimation from Its Shadow. In: *The Astrophysical Journal* 892 (2020), mar, Nr. 2, S. 78. – URL https://dx.doi.org/10.3847/1538-4357/ab77b0

[12] NEHER MESTRE, Narcís: *Black Hole Shadows: Schwarzschild and Reissner-Nordström (anti-)dSitter.* 2023. – URL `https://diposit.ub.edu/dspace/bitstream/2445/201287/1/NEHER%20MESTRE%20NARC%C3%8DS_7934140.pdf`

[13] NEWMAN, E T. ; COUCH, E ; CHINNAPARED, K ; EXTON, A ; PRAKASH, A ; TORRENCE, R: Metric of a Rotating, Charged Mass. In: *Journal of Mathematical Physics (New York) (U.S.)* 6 (1965), 6, S. 918–919. – URL `https://www.osti.gov/biblio/4590009`

[14] NORDEBO, Jonatan: *The Reissner-Nordström metric.* 2016. – URL `https://www.diva-portal.org/smash/get/diva2:912393/FULLTEXT01.pdf`

[15] REISSNER, Hans: Über die Eigengravitation des elektrischen Feldes nach der Einsteinschen Theorie. In: *Annalen der Physik* 355 (1916), S. 106–120

[16] SHAIKH, Rajibul: Testing black hole mimickers with the Event Horizon Telescope image of Sagittarius A. In: *Monthly Notices of the Royal Astronomical Society* 523 (2023), Nr. 1, S. 375–384

[17] SHAIKH, Rajibul ; PAUL, Suvankar ; BANERJEE, Pritam ; SARKAR, Tapobrata: Shadows and thin accretion disk images of the γ-metric. In: *The European Physical Journal C* 82 (2022), Nr. 8, S. 696

[18] SNEPPEN, Albert: Divergent reflections around the photon sphere of a black hole. In: *Scientific Reports* 11 (2021), Juli, Nr. 1. – URL `http://dx.doi.org/10.1038/s41598-021-93595-w`. – ISSN 2045-2322

[19] TAMBURINI, Fabrizio ; THIDÉ, Bo ; DELLA VALLE, Massimo: Measurement of the spin of the M87 black hole from its observed twisted light. In: *Monthly Notices of the Royal Astronomical Society: Letters* 492 (2019), 11, Nr. 1, S. L22–L27. – URL `https://doi.org/10.1093/mnrasl/slz176`. – ISSN 1745-3925

[20] VAGNOZZI, Sunny ; ROY, Rittick ; TSAI, Yu-Dai ; VISINELLI, Luca ; AFRIN, Misba ; ALLAHYARI, Alireza ; BAMBHANIYA, Parth ; DEY, Dipanjan ; GHOSH, Sushant G. ; JOSHI, Pankaj S. ; JUSUFI, Kimet ; KHODADI, Mohsen ; WALIA, Rahul K. ; ÖVGÜN, Ali ; BAMBI, Cosimo: Horizon-scale tests of gravity theories and fundamental physics from the Event Horizon Telescope image of Sagittarius A^*. In: *Classical and Quantum Gravity* 40 (2023), jul, Nr. 16, S. 165007. – URL `https://dx.doi.org/10.1088/1361-6382/acd97b`

[21] VINCENT, F. H. ; WIELGUS, M. ; ABRAMOWICZ, M. A. ; GOURGOULHON, E. ; LASOTA, J.-P. ; PAUMARD, T. ; PERRIN, G.: Geometric modeling of M87* as a Kerr black hole or a non-Kerr compact object. In: *Astronomy & Astrophysics* (2020). – URL `https://arxiv.org/abs/2002.09226`

[22] VIRBHADRA, KS: Directional naked singularity in General Relativity. In: *arXiv preprint gr-qc/9606004* (1996)

[23] WIKIPEDIA: *Charged black hole.* – URL https://en.wikipedia.org/wiki/Charged_black_hole. – Online; accessed 17th January 2024

[24] WIKIPEDIA: *Reissner–Nordström metric.* – URL https://en.wikipedia.org/wiki/Reissner%E2%80%93Nordstr%C3%B6m_metric. – Online; accessed 12th January 2024